Accurate Angular Inference for 802.11ad Devices Using Beam-Specific Measurements

Haichuan Ding and Kang G. Shin, *Life Fellow, IEEE*

Abstract—Due to their sparsity, 60GHz channels are characterized by a few dominant paths. Knowing the angular information of their dominant paths, we can develop various applications, such as the prediction of link performance and the tracking of 802.11ad devices. Although they are equipped with phased arrays, the angular inference for 802.11ad devices is still challenging due to their limited number of RF chains and limited phase control capabilities. Considering the beam sweeping operation and the high communication bandwidth of 802.11ad devices, we propose variation-based angle estimation (VAE), called VAE-CIR, by utilizing beam-specific channel impulse responses (CIRs) measured under different beams and the directional gains of the corresponding beams to infer the angular information of dominant paths. Unlike state-of-the-arts, VAE-CIR exploits the variations between different beam-specific CIRs for angular inference and provides a performance guarantee in the high signal-to-noise-ratio regime. To evaluate VAE-CIR, we generate the beam-specific CIRs by simulating the beam sweeping of 802.11ad devices with the beam patterns measured on off-the-shelf 802.11ad devices. The 60GHz channel is generated via a ray-tracing-based simulator and the CIRs are extracted via channel estimation based on Golay sequences. Through extensive experiments, VAE-CIR is shown to achieve more accurate angle estimation than existing schemes.

Index Terms—mmWave communications, IEEE 802.11ad, angular inference

1 Introduction

The completion of the 802.11ad standard and its device commercialization have led to various research efforts to either improve the communication performance of 60GHz devices, such as link performance prediction, access point (AP) deployment, and seamless indoor multi-Gbps wireless connectivity, or develop novel applications with these devices, such as single AP decimeter-level localization [1], [2], [3], [4], [5]. All these applications usually rely on the length and angular information of strong signal (or *dominant*) paths in the sparse 60GHz channel. Since this path information is often unavailable, we must be able to effectively infer such information for which angular information serves as the starting point.

As demonstrated in prior studies, the starting point for inferring path information is the collection of angular information — such as angles of departure (AODs) and angles of arrival (AOAs) — of dominant paths [1], [2], [3], [4], [5]. For example, when the 802.11ad device is $5m$ away from the AP, the angle estimation error should be less than 6° and 3° to achieve a localization accuracy of 5 decimeters and 2 decimeters, respectively. To predict the received signal strength with a median prediction error of $2.8dB$, the AOAs/AODs of dominant paths should be estimated with an average error of less than 6° [1]. Unfortunately, because of their irregular beam patterns and limited number of radio frequency (RF) chains, inferring angular information with the desired level of accuracy is not easy for 802.11ad devices. On the one hand, for cost reasons, phased arrays on off-the-shelf 802.11ad devices only support 2 to 4-bit phase control [6]. As reported in [7], to limit overhead and enable fast network discovery and user association, the beams of 802.11ad devices should cover desired directions with specific beamwidth. To meet these requirements with limited phase control capability, the beams implemented on 802.11ad devices often have multiple strong side lobes [7], [8]. In the presence of multipath propagation, such irregular beam patterns make it difficult for 802.11ad devices to directly learn angular information from, for example, sector level sweep (SLS). On the other hand, due to the limited number of RF chains, existing direction-estimation schemes are not applicable to off-the-shelf 802.11ad devices. As reported in [1], 802.11ad devices adopt analog phased arrays and the signals received at different antenna elements are mixed at the output of the RF chain. Since most existing direction-estimation schemes require the knowledge of signal received at each antenna element, they are not applicable to millimeter wave (mmWave) devices with analog phased arrays. Although a few direction-estimation schemes have been proposed for antenna arrays with a hybrid beamforming architecture, they cannot be directly integrated into 802.11ad devices which are equipped with only a single RF chain.

In view of the above-mentioned challenges, we develop a variation-based angle estimation (VAE), called VAE-CIR, to enable accurate angular inference for 802.11ad devices without any assumptions on beam patterns and the number of RF chains. The basic idea of VAE-CIR is to exploit the variations in beam-specific channel impulse responses (CIRs) measured under different beams during, for example, beam sweeping, to gradually narrow down the AOAs/AODs of

- *Haichuan Ding is with the School of Cyberspace Science and Technology, Beijing Institute of Technology, Beijing 100081, China. E-mail: hcding@bit.edu.cn.*
- *Kang G. Shin is with the Department of Electrical Engineering and Computer Science, University of Michigan, Ann Arbor, MI 48109 USA. E-mail: kgshin@umich.edu.*

Manuscript received 18 May 2020; revised 24 July 2020; accepted 30 July 2020. Date of publication 11 Aug. 2020; date of current version 3 Feb. 2022. (Corresponding author: Haichuan Ding.)
Digital Object Identifier no. 10.1109/TMC.2020.3015936

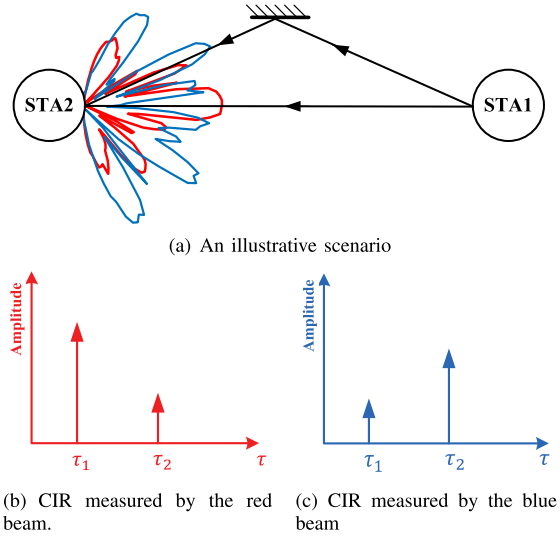

(a) An illustrative scenario

(b) CIR measured by the red beam.

(c) CIR measured by the blue beam

Fig. 1. Motivation for VAE-CIR. The red and blue beams are measured from Dell E7440 notebook which is equipped with antenna arrays to operate in 60GHz bands [10].

different paths. Specifically, for each path of interest, VAE-CIR maintains the score for each direction and utilizes the beam-specific CIR measurements under different beam patterns to update the score. Instead of updating the score of each direction based on the absolute CIR measurement under each individual beam, VAE-CIR updates the score for each direction based on the variations between every two CIRs measured using different beams, and the direction where the variation in the directional gain better matches that in the CIR will be assigned a lower score increase. Then, VAE-CIR selects the direction with the lowest score, namely, the direction in which the variations of the directional gain best match the variations in the CIR component, as the estimated angle for the path of interest. The rationale behind VAE-CIR can be illustrated through the example in Fig. 1a where the signal from STA1 reaches STA2 through a light-of-sight (LOS) and a reflected paths and these two paths are resolvable in the CIR measured at STA2. The CIRs measured under the red and blue beams are shown in Figs. 1b and 1c. The CIR component corresponding to the LOS path arrives at τ_1 and that corresponding to the reflected path arrives at τ_2. Since those two beams encounter the same set of signal paths, when STA2 switches from the red beam to the blue beam, the variation in each CIR component is a result of the variations in the directional gain (i.e., the beamforming gain) along the AOA/AOD of its corresponding path. In other words, when STA2 changes its beam, the AOA/AOD of each path should provide the best match between the variations in the directional gain and those in its corresponding CIR component.

In practice, the collection of the aforementioned beam-specific CIRs and thus VAE-CIR is enabled by the characteristics of 802.11ad frames and the measurement process, like beam sweeping, inherent in 802.11ad operation. According to [9], each 802.11ad frame begins with a short training field (STF) and a channel estimation (CE) field, which allow 802.11ad devices to acquire the corresponding CIR. Moreover, since the 802.11ad frames are delivered via a spectrum of $\geq 1760MHz$ bandwidth, two path components are resolvable for 802.11ad devices as long as their arrival times differ by $\geq 0.57ns$. In other words, two paths are resolvable for 802.11ad devices as long as their lengths differ by $\geq 0.17m$. Given the sparsity of mmWave channels, each dominant component in the CIR is highly likely to correspond to one of the dominant propagation paths between the transmitter and the receiver. That is, each dominant CIR component is highly likely to be completely determined by a dominant path, thus providing us information to infer the AOA/AOD of the corresponding path.

This paper makes the following contributions.

- A novel study of the angular inference for 802.11ad devices based on wireless measurements. Unlike prior work, we propose to not directly utilize each CIR component but employ its variations under different beams to infer the angle of each path.
- Design of VAE-CIR which exploits the variations in every two CIR measurements to infer the AOA/AOD of dominant paths. For a specific path, VAE-CIR exploits the variations in its corresponding CIR component between every two measurements to update the score assigned to different directions and the inferred AOA/AOD is the direction with the lowest final score. VAE-CIR allows us to flexibly weight the contribution of every two CIR measurements to the score. For example, a lower weight can be assigned when the amplitude of the interested CIR component is below a certain threshold in at least one of the two CIR measurements. This way we are able to limit the impact of noise on AOA/AOD inference since the accuracy of weak CIR measurements is more prone to noise. Moreover, VAE-CIR is proved to provide a performance guarantee in the high signal-to-noise-ratio (SNR) regime.
- Extensive simulation to evaluate effectiveness of VAE-CIR. We generate the transmit signals and implement the channel estimation based on Golay sequences for CIR extraction by following the IEEE 802.11ad standard. Using the beam pattern measured on the off-the-shelf 802.11ad devices and the channel model approved by IEEE 802.11 Task Group ad, we demonstrate the superiority of VAE-CIR to state-of-the-arts.

2 Related Work

Several direction-estimation schemes have recently been proposed for 802.11ad devices based on a single RF chain and analog arrays. Wei *et al.* [1] exploited the orthogonality within the codebook to map the output of the RF chain to the signals received at different antenna elements and used the MUSIC algorithm to estimate the AOAs of different paths. In their scheme, the device receives the incoming signal using different weight vectors (i.e., beam patterns) and isolates the signal received at each antenna element through a matrix inversion. As pointed out in [5], to make this scheme effective, we should ensure that exactly the same signal is sampled by all of the adopted beam patterns, thus limiting its applicability. Furthermore, the placement and enclosures of the phased array antenna might affect its

radiation pattern, making the relationship between weight vectors and directional gains invalid, and thus adversely impacting the performance of the AOA estimation schemes based on weight vectors [8]. So, most existing direction estimation schemes for 802.11ad devices exploit the correlation between wireless measurements made under different beams and the directional gains of the corresponding beams for angular inference [4], [5], [11]. Steinmetzer *et al.* [11] proposed a direction estimation scheme based on received signal strength (RSS) to infer the AOA of a dominant path. In that scheme, multiple RSS measurements are made using different beams, and the estimated AOA is the direction that provides the best match between the directional gains and the RSS measurements. Although its effectiveness has been demonstrated in a specific environment, the experimental results in [5] show this RSS-based scheme to be highly inaccurate in a different environment due to irregular beam patterns and multipath propagation. In this case, the RSS not only depends on the path of interest but also is affected by the signals received from other paths.

This observation motivates Ghasempour *et al.* [4] and Pefkianakis *et al.* [5] to propose two direction-estimation schemes by exploiting the measured CIR, instead of the RSS, for angular inference [4], [5]. In these two schemes, CIR components are first mapped to dominant paths through their time of arrival. Then, the corresponding CIR components measured under different beams are used to gradually refine the AOA/AOD estimates of the paths of interest. For each dominant path, the scheme in [4] maintains a score for each direction with initial value 0. Once a new CIR measurement comes in, the score of each direction is updated depending on whether the desired CIR component is received or not, as well as the directional gain of the adopted beam pattern. When the measurement process completes, the direction with the highest score will be considered as the AOA of the corresponding path. The authors of [5] adopted a similar procedure to estimate the AOD of the line-of-sight (LOS) path by utilizing the CIR feedback from the receiver. To improve the accuracy of AOD estimation further, they selected a few CIR measurements with the strongest LOS components for AOD estimation and weighted the contribution of each CIR measurement with the amplitude of its LOS component. They then chose the estimated AOD to be the center of the direction interval spanned by a few directions with the highest scores. Despite the differences, both of these schemes rely on a hidden assumption that, if a CIR component is received under a beam, the angle of the corresponding path is more likely to be along the direction with a higher directional gain. As a result, once the desired CIR component is measured under a beam, they always assign the highest score increase to the direction with the highest directional gain. However, the reception of a CIR component only implies that the directional gain along the AOA/AOD of the corresponding path is higher than a certain threshold, rather than that the AOA/AOD of this path is along the direction with the highest gain. Blindly assigning higher score increments to the directions with higher directional gains might lead to large estimation errors.

As seen from the above discussions, despite the various angle estimation schemes proposed thus far, accurate AOA/AOD estimation for 802.11ad devices is still lacking. This observation motivates our proposal of VAE-CIR. Instead of always assigning the lowest increase of score to the direction with the highest directional gain,[1] VAE-CIR assigns the lowest increase of score to the direction yielding the best match between the variations in directional gains and those in the corresponding CIR measurements, which would lead to accurate direction estimation. Besides, unlike existing schemes where only heuristics are provided, VAE-CIR is proved to offer a performance guarantee in the high SNR regime.

3 Beam-Specific CIR and Channel Estimation

3.1 Beam-Specific CIR

To compensate high path loss and facilitate high speed transmissions, mmWave communication devices exploit phased arrays and beamforming to concentrate energy in the desired directions. Due to the constraints on hardware implementation, 802.11ad devices adopt an analog beamforming architecture where each antenna is connected with a phase shifter and beamforming is performed in the analog domain with these phase shifters. This analog beamforming architecture cannot simultaneously support more than one beam, and can steer the beam to different directions by controlling the amount of shift in each phase shifter [12]. Due to the use of beamforming, the CIR observed at the receiver depends on both the underlying signal paths and the radiation pattern of the adopted beam. Denoting the equivalent lowpass representation of the continuous-time CIR as $h(t)$ [13], we have

$$h(t) = \sum_{k=1}^{K} \alpha_k \mathcal{G}_m(\vartheta_k) G_l(\theta_k) \delta(t - \tau_k), \tag{1}$$

where K is the total number of underlying signal paths, α_k and τ_k are the complex path gain and the delay of the kth path, respectively. ϑ_k is the AOD of the kth path at the transmitter and $\mathcal{G}_m(\vartheta_k)$ is the beamforming gain along the spatial direction ϑ_k when the transmitter uses its mth beam for transmissions. θ_k is the AOA of the kth path at the receiver and $G_l(\theta_k)$ is the beamforming gain along direction θ_k when the receiver employs its lth beam for reception. Each summand in Eq. (1) corresponds to a CIR component. Let h_k be the kth CIR component and $h_k(l)$ be the kth CIR component measured using the lth receiving beam. When the underlying signal path remains the same, the amplitude of each CIR component, $|h_k|$, will track the changes of directional gains. For example, if the receiver switches to the $(l+1)$-th beam, we have $|h_k| = |h_k(l+1)| = |\alpha_k \mathcal{G}_m(\vartheta_k) G_{l+1}(\theta_k)|$ and $|h_k(l+1)|/|h_k(l)| = |G_{l+1}(\theta_k)|/|G_l(\theta_k)|$. In other words, the variations in the directional gain along the AOA θ_k of a path matches the variations in the amplitude of its corresponding CIR component h_k. This observation motivates VAE-CIR which we introduce in the next section.

3.2 Channel Estimation in 802.11ad

According to the IEEE 802.11ad standard, each physical layer (PHY) protocol data unit (PPDU) contains a CE field right next to the STF. 802.11ad PHY supports two

1. VAE-CIR takes the direction with the lowest final score as the estimated AOA/AOD.

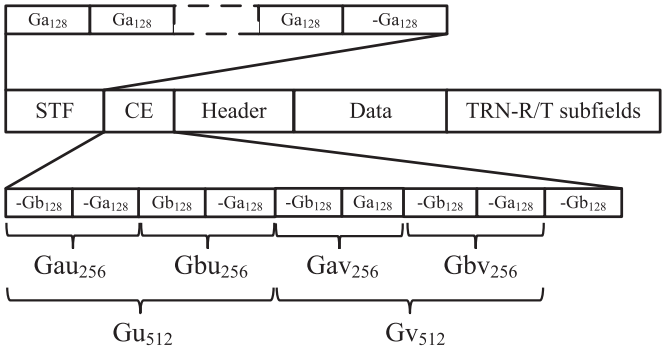

Fig. 2. The structure of a typical 802.11ad PPDU.

modulation methods — control modulation and single carrier (SC) modulation — which share a common preamble structure [9], [14]. The structure of a typical 802.11ad PPDU is shown in Fig. 2, where $Gau_{256}[n]$, $Gbu_{256}[n]$, $Gav_{256}[n]$, $Gbv_{256}[n]$ are Golay sequences of length 256. From Fig. 2, each of these sequences is obtained by concatenating two Golay sequences of length 128. $Ga_{128}(n)$ and $Gb_{128}(n)$ are two Golay sequences of length 128 defined in subclause 20.10 of [14]. $Gau_{256}(n)$ and $Gbu_{256}(n)$ are complementary sequences. $Gav_{256}(n)$ and $Gbv_{256}(n)$ are complementary sequences. $Ga_{128}(n)$ and $Gb_{128}(n)$ are complementary sequences. The autocorrelation property of these Golay sequences is exploited in 802.11ad for channel estimation [15], [16]. Clearly from Fig. 2, both the STF and CE field are built up from Golay sequences. Each STF ends with $-Ga_{128}(n)$, and each CE field ends with $-Gb_{128}(n)$, which facilitates the creation of a length-127 zero-correlation zones as discussed below [17]. The STF and CE fields are modulated prior to transmission using $\pi/2$-BPSK. We use $\widetilde{Gau}_{256}[n]$ and $\widetilde{Gbu}_{256}[n]$ to denote $Gau_{256}[n]$ and $Gbu_{256}[n]$ after constellation mapping.

Let $s(t)$ be the transmitted preamble before upconversion. Then, we have

$$s(t) = \sum_{n=0}^{1279} s[n](g * h_T)(t - nT_c), \tag{2}$$

where $s[n]$ is a sequence obtained by sequentially concatenating $-\widetilde{Ga}_{128}$, $\widetilde{Gu}_{512}$, $\widetilde{Gv}_{512}$, and $-\widetilde{Gb}_{128}$, $h_T(t)$ represents the transmit shaping filter, and T_c is the chip time. $T_c = 0.57ns$ for control and SC PHY. $g(t) = u(t) - u(t - T_c)$, where $u(t)$ is the unit step function defined in [18]. $*$ in Eq. (2) represents the operation of convolution. It should be noted that, for ease of presentation, we only consider the part of the preamble related to channel estimation in Eq. (2). Then, the received signal after going through the wireless channel, downcoversion, and the anti-aliasing filter is

$$r(t) = \sum_{k=1}^{K} h_k(s * h_R)(t - \tau_k) + z(t), \tag{3}$$

where h_k is the kth CIR component defined in the last subsection, $h_R(t)$ is the impulse response of the anti-aliasing filter at the receiver, and $z(t)$ is the additive noise. Suppose $(h_T * h_R)(t)$ is designed to have a flat frequency response with magnitude 1 in the band of interest, the received signal sampled at a rate of $1/T_c$ is

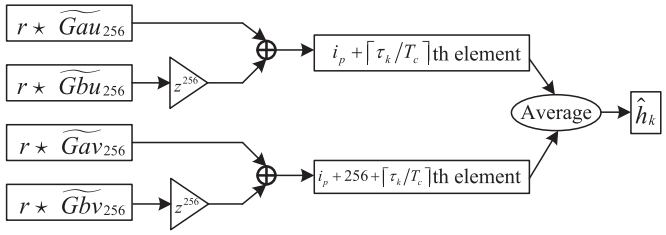

Fig. 3. Golay sequence based estimation for the kth CIR component. z^{256} is the delay operator.

$$r(nT_c) = \sum_{k=1}^{K} h_k \sum_{j=0}^{1279} s[j]g(nT_c - \tau_k - jT_c) + z(nT_c). \tag{4}$$

Let $r[n] = r(nT_c)$ and $z[n] = z(nT_c)$, we have

$$r[n] = \sum_{k=1}^{K} h_k s[n - \lceil \tau_k / T_c \rceil] + z[n], \tag{5}$$

where $\lceil . \rceil$ is the ceiling function. To obtain the estimated CIR, $r[n]$ is first correlated with $\widetilde{Gau}_{256}$, $\widetilde{Gbu}_{256}$, $\widetilde{Gav}_{256}$, and $\widetilde{Gbv}_{256}$. Specifically, we have

$$\begin{aligned}\left(r^{\star}\widetilde{Gau}_{256}\right)[i] = &\sum_{k=1}^{K} h_k\left(s^{\star}\widetilde{Gau}_{256}\right)[i - \lceil \tau_k/T_c \rceil] \\ &+ \left(z^{\star}\widetilde{Gau}_{256}\right)[i],\end{aligned} \tag{6}$$

where * is the correlation operator, and

$$\begin{aligned}&\left(s^{\star}\widetilde{Gau}_{256}\right)[i] \\ &= \begin{cases} \sum_{n=\max\{-i,0\}}^{\min\{\ell_s - i, 255\}} s[n]\widetilde{Gau}_{256}[n-i] & -255 \le i \le \ell_s \\ 0 & o.w. \end{cases}.\end{aligned} \tag{7}$$

Similar results can be obtained for $\widetilde{Gbu}_{256}$, $\widetilde{Gav}_{256}$, and $\widetilde{Gbv}_{256}$.

As shown in Fig. 3, $(r^{\star}\widetilde{Gau}_{256})[i]$ is then combined with $(r^{\star}\widetilde{Gbu}_{256})[i]$, $(r^{\star}\widetilde{Gav}_{256})[i]$, and $(r^{\star}\widetilde{Gbv}_{256})[i]$ to obtain the estimated CIR. By adding $(r^{\star}\widetilde{Gau}_{256})[i]$ and $(r^{\star}\widetilde{Gbu}_{256})[i + 256]$, we have

$$R_{ru}[i] = \sum_{k=1}^{K} h_k R_{su}[i - \lceil \tau_k / T_c \rceil] + \widetilde{z}[i], \tag{8}$$

where $\widetilde{z}[i]$ is the noise after correlation operation and

$$\begin{aligned}R_{ru}[i] &= \left(r^{\star}\widetilde{Gau}_{256}\right)[i] + \left(r^{\star}\widetilde{Gbu}_{256}\right)[i + 256], \\ R_{su}[i] &= \left(s^{\star}\widetilde{Gau}_{256}\right)[i] + \left(s^{\star}\widetilde{Gbu}_{256}\right)[i + 256].\end{aligned} \tag{9}$$

Clearly from Eq. (8), the value of $R_{ru}[i]$ is closely related to that of $R_{su}[i]$. Let $R_{sau}[i] = (s^{\star}\widetilde{Gau}_{256})[i]$, and $R_{sbu}[i] = (s^{\star}\widetilde{Gbu}_{256})[i]$. By exploiting the autocorrelation property of Golay sequences, we have

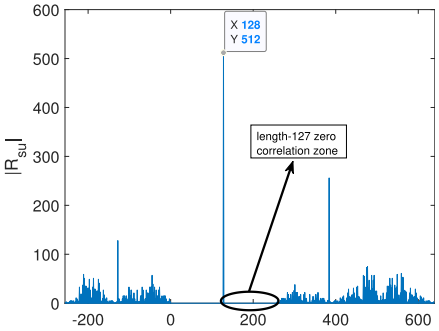

Fig. 4. The value of $|R_{su}[i]|$. We have $i_p = 128$ since $\widetilde{Gau}_{256}$ starts at the 128th element of s. A length-127 zero correlation zone can be clearly seen before and after the index of 128.

$$|R_{su}[i]| = |R_{sau}[i] + R_{sbu}[i+256]| = \begin{cases} 512 & i = 128 \\ 0 & 0 \le i \le 255, i \ne 128 \end{cases}, \quad (10)$$

From Eq. (10), $|R_{su}[i]|$ has a peak at the index $i_p = 128$ where $\widetilde{Gau}_{256}$ aligns with $\widetilde{Gau}_{256}$ in s, and there is a length-127 zero-correlation zone before and after the peak. This matches the result in Fig. 4 well.

Noting that $R_{su}[i - \lceil \tau_k/T_c \rceil]$ is a shifted version of $R_{su}[i]$, $|R_{su}[i - \lceil \tau_k/T_c \rceil]|$ has a peak at location $i_p(k) = i_p + \lceil \tau_k/T_c \rceil$. Without of loss generality, let us assume $\lceil \tau_{k'}/T_c \rceil \ne \lceil \tau_k/T_c \rceil$ if $k' \ne k$ and $|\tau_K - \tau_1| \le 128T_c$. Then, if the noise is neglected, we get $\left|R_{ru}\left[i_p + \lceil \tau_k/T_c \rceil\right]\right| = 512|h_k|$. In other words, we can recover the kth CIR component by extracting the $\left(i_p + \lceil \tau_k/T_c \rceil\right)$-th element in $R_{ru}[i]$ through $\widehat{h}_k^u = R_{ru}\left[i_p + \lceil \tau_k/T_c \rceil\right]/512$, where $\widehat{h}_k^u$ represents the estimate of the kth CIR component. Following the same procedure, we can obtain another estimate of the kth CIR component, denoted as $\widehat{h}_k^v$, by correlating $r[n]$ with $\widetilde{Gav}_{256}$ and $\widetilde{Gbv}_{256}$. To reduce the impact of noise, we average $\widehat{h}_k^u$ and $\widehat{h}_k^v$ to obtain the final estimate for the kth CIR component as $\widehat{h}_k = (\widehat{h}_k^u + \widehat{h}_k^v)/2$.

For ease of presentation, we assume the signal is transmitted with unit power in the above discussion. The effect of actual transmit power P_t can be easily incorporated by scaling h_k with a factor of $\sqrt{P_t}$. In practice, the quality of the estimated CIR component $\widehat{h}_k$ is affected by noise and other non-resolvable CIR components with respect to the kth CIR component, which could, in turn, affect the performance of VAE-CIR. As mentioned in [19], the channel at 60GHz is inherently sparse with a few dominant paths. Thanks to the high transmission bandwidth, two CIR components can be resolved as long as the difference in their time of arrival is larger than $0.57ns$. Thus, the impact of non-resolvable CIR components on $\widehat{h}_k$ is expected to be limited if it corresponds to a dominant path. In Section 5, we will discuss how noise affects the performance of VAE-CIR and show that non-resolvable CIR components have only limited effect on VAE-CIR.

4 Design of VAE-CIR

VAE-CIR addresses the problem of estimating the AOA/AOD of a specific dominant path, given a set of beam-specific CIR measurements. How to identify the dominant paths of a channel is out of the scope of VAE-CIR. As mentioned in [4], [5], the dominant paths of a channel can be identified by detecting and aggregating the peaks in the given set of beam-specific CIR measurements. Without loss of generality, we assume K dominant paths, indexed as $\{1, \ldots, \mathrm{K}\}$, are identified from the given set of beam-specific CIR measurements, and we are interested in the angular information of the κ-th ($\kappa \in \{1, \ldots, \mathrm{K}\}$) dominant path. For simplicity, we call the CIR component corresponding to the κ-th dominant path as the κ-th dominant CIR component.

As mentioned before, VAE-CIR exploits the CIR measured under different beams to infer the AOAs/AODs of dominant paths. These CIR measurements can be collected using, for example, sector sweep (SSW) frames during the sector-level sweep phase or a specific beam-sweeping process [3], [4], [5]. In general, the beam-sweeping is carried out in one or multiple stages. During each stage, one party fixes its beam pattern and the other party sweeps through different beams. For ease of presentation, we focus on AOA estimation in the following development and thus are interested in the case where the transmitter fixes its beam and the receiver receives the beam training frames, such as the SSW frames, with different beams. By exploiting channel reciprocity, VAE-CIR presented in this section can also be applied in AOD inference using the transmitter-side beam sweeping. Suppose the receiver can sweep through a maximum of L beams, and thus we have the CIRs measured under L different beams. Let $h_\kappa(l)$ be the value of the κ-th dominant CIR component when the lth beam is used for reception. As shown in [4], [5], the estimate of $h_\kappa(l)$, denoted as $\widehat{h}_\kappa(l)$, can be extracted from the estimated CIR under the lth receiving beam based on the time of arrival of the κ-th dominant path from aggregated CIR measurements.

Let θ_κ be the AOA of the κ-th dominant path. To infer θ_κ from $\widehat{h}_\kappa(l)$'s, we need to draw a quantity from $\widehat{h}_\kappa(l)$'s so that it is determined solely by θ_κ. Clearly from Eq. (1), it is difficult to directly infer θ_κ from the amplitudes of $h_\kappa(l)$'s since they are also affected by many other factors, such as the path gain and the directional gain of the transmit beam. Notice that, when the transmit power and transmit beam pattern are fixed, $h_\kappa(l)$'s satisfy:

$$|h_\kappa(l_1)|/|h_\kappa(l_2)| = \left|G_{l_1}(\theta_\kappa)\right|/\left|G_{l_2}(\theta_\kappa)\right|. \quad (11)$$

In other words, when the l_1-th and the l_2-th beams are used for reception, the ratio of $|h_\kappa(l_1)|$ to $|h_\kappa(l_2)|$ is completely determined by θ_κ. This observation leads us to use the ratio between $\left|\widehat{h}_\kappa(l)\right|$'s, instead of their absolute values, for AOA estimation.

Due to the very irregular beam pattern of 802.11ad devices, it is challenging to analytically derive the inverse function of $\left|G_{l_1}(\theta_\kappa)\right|/\left|G_{l_2}(\theta_\kappa)\right|$ for AOA estimation. In view of Eq. (11), we address this challenge by searching for the direction which minimizes the difference between the left-hand and right-hand sides of Eq. (11). Specifically, given $\widehat{h}_\kappa(l_1)$ and $\widehat{h}_\kappa(l_2)$, we have

$$\widehat{\theta}_\kappa = \arg\min_{\theta \in \Theta} \left| \frac{\left|\widehat{h}_\kappa(l_1)\right|}{\left|\widehat{h}_\kappa(l_2)\right|} - \frac{\left|G_{l_1}(\theta)\right|}{\left|G_{l_2}(\theta)\right|} \right|, \quad (12)$$

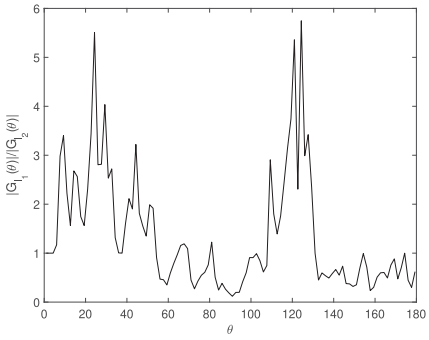

Fig. 5. The values of $|G_{l_1}(\theta)|/|G_{l_2}(\theta)|$ under different values of θ. The results are obtained based on the 2nd and 3rd beams swept by Dell D5000 Docking station during sector level sweep.

where $\widehat{\theta}_\kappa$ is the estimated AOA of the κth dominant path, and Θ represents the search space which could be determined by the filed of view (FoV) of the antenna array [20]. As shown in Fig. 5, multiple values of θ could lead to the same value of $\left|G_{l_1}(\theta)\right|/\left|G_{l_2}(\theta)\right|$. This ambiguity in AOA estimation can be resolved by aggregating the measurements from multiple beam pairs. Specifically, when new CIR measurements are available, we can combine them with $\widehat{h}_\kappa(l_1)$ and $\widehat{h}_\kappa(l_2)$ to refine our estimation, which leads to VAE-CIR.

To infer the AOA of the κ-th path, VAE-CIR maintains a score for each direction. Since the goal of VAE-CIR is to find the direction where the ratios between directional gains best match those between the corresponding beam-specific CIR measurements, we define the score function by generalizing (12) to account for the beam-specific CIR measurements from L different beams. VAE-CIR does not assume the order in which $\widehat{h}_\kappa(1),\ldots,\widehat{h}_\kappa(L)$ are used for updating the score, but, in this section, we assume they are sequentially used for score updating for ease of presentation. Let $s_\kappa^\ell(\theta)$ be the score assigned to each direction based on $\widehat{h}_\kappa(1),\ldots,\widehat{h}_\kappa(\ell)$, where $\ell\in\{1,\ldots,L\}$ is the beam index. Observing that the score is updated based on the variation between different CIR measurements, we have $s_\kappa^1(\theta)=0,\forall\theta\in\Theta$. For $\ell\geq 2$, $s_\kappa^\ell(\theta)$ can be obtained from $s_\kappa^{\ell-1}(\theta)$ using $\widehat{h}_\kappa(\ell)$ as

$$s_\kappa^\ell(\theta)=\begin{cases} s_\kappa^{\ell-1}(\theta)+\sum_{l\in\mathcal{L}}\left\{\begin{array}{c}\alpha(\ell,l,\kappa,\theta)\times\\ \left|\frac{\left|\widehat{h}_\kappa(\ell)\right|}{\left|\widehat{h}_\kappa(l)\right|}-\frac{|G_\ell(\theta)|}{|G_l(\theta)|}\right|\end{array}\right\} & \mathcal{L}\neq\emptyset,\ell\notin\mathcal{L}\\ s_\kappa(\theta) & \text{otherwise}\end{cases}, \tag{13}$$

where $\mathcal{L}$ is the set of receiving beams used in the previous CIR measurement, and $\emptyset$ is an empty set. Initially, we have $\mathcal{L}=\{1\}$. $\alpha(\ell,l,\kappa,\theta)$'s are weight factors which allow us to weight the contribution of every two CIR measurements based on the corresponding beams, the considered direction, and the dominant path of interest. In this paper, we set $\alpha(\ell,l,\kappa,\theta)$ as $1\left(\left|\widehat{h}_\kappa(\ell)\right|\geq\hbar\right)1\left(\left|\widehat{h}_\kappa(l)\right|\geq\hbar\right)$, where $1(.)$ is the indicator function. $\hbar$ is a threshold and can be set to, for example, $\nu\left|\widehat{h}\right|_\kappa^{\max}$, where $\nu\in[0,1]$, and $\left|\widehat{h}\right|_\kappa^{\max}=\max_{l\in\{1,\cdots,L\}}\left|\widehat{h}_\kappa(l)\right|$. We adopt such weight factors since the value of $\left|\widehat{h}_\kappa(l)\right|$ cannot be fully trusted when it is too small. On the one hand, the small $\left|\widehat{h}_\kappa(l)\right|$ could be caused by either a low beamforming gain along θ_κ or an abrupt blockage of the κ-th dominant path. On the other hand, a small $\left|\widehat{h}_\kappa(l)\right|$ is more susceptible to noise and might not be able to accurately track the variations in $|h_\kappa(l)|$. In other words, when either $\left|\widehat{h}_\kappa(\ell)\right|$ or $\left|\widehat{h}_\kappa(l)\right|$ is small, the variation in the beamforming gain along θ_κ might not be the major reason for the variation in $\left|\hat{h}_\kappa(\ell)\right|/\left|\hat{h}_\kappa(l)\right|$, and applying these $\left|\widehat{h}_\kappa(l)\right|$'s in AOA estimation could adversely affect the accuracy. Besides limiting the impact of small $\left|\widehat{h}_\kappa(l)\right|$'s, $\alpha(\ell,l,\kappa,\theta)$ also allows VAE-CIR to incorporate prior information. For example, if θ_κ is known to be within a direction range $\widetilde{\Theta}$, we can exploit such information for AOA estimation by assigning 1 to $\alpha(\ell,l,\kappa,\theta),\forall\theta\in\widetilde{\Theta}$, and 0 otherwise.

Once the updated score $s_\kappa^\ell(\theta)$ is obtained, we update $\mathcal{L}$ as

$$\mathcal{L}=\mathcal{L}\cup\{\ell\}. \tag{14}$$

After going through all L CIR measurements, VAE-CIR outputs the estimated AOA of the κ-th dominant path as[2]

$$\widehat{\theta}_\kappa=\arg\min_{\theta\in\Theta}s_\kappa^L(\theta). \tag{15}$$

VAE-CIR is summarized in Algorithm 1. As shown in Algorithm 1, the complexity of VAE-CIR mainly comes from updating the score function $s_\kappa^\ell(\theta)$ based on (13). When L beams are used for angular inference, (13) will be evaluated $L|\Theta|$ times, where $|\Theta|$ is the cardinality of the search space Θ. Since each evaluation of (13) has a running time of $O(L)$, the proposed solution has a complexity of $O(L^2|\Theta|)$.

Algorithm 1. VAE-CIR

Input: $\widehat{h}_\kappa(l), l\in\{1,\ldots,L\}, G_l(\theta), l\in\{1,\ldots,L\}, \theta\in\Theta, \Theta, \hbar$
Output: $\widehat{\theta}_\kappa$
1: $s_\kappa^1(\theta)=0,\forall\theta\in\Theta,\mathcal{L}=\{1\}$
2: **for** ℓ=2 to L **do**
3: **for** $l\in\mathcal{L}$ **do**
4: Determine $\alpha(\ell,l,\kappa,\theta)$ based on $\widehat{h}_\kappa(\ell)$, $\widehat{h}_\kappa(l)$, and other information (e.g., $\hbar$ in this paper)
5: **end for**
6: $\forall\theta\in\Theta$, update $s_\kappa^{\ell-1}(\theta)$ to $s_\kappa^\ell(\theta)$ according to Eq. (13)
7: $\mathcal{L}=\mathcal{L}\cup\{\ell\}$
8: **end for**
9: $\widehat{\theta}_\kappa=\arg\min_{\theta\in\Theta}s_\kappa^L(\theta)$

The following lemma provides a hint on the effectiveness of VAE-CIR.

Lemma 1. *In the high SNR regime, θ_κ minimizes $s_\kappa^L(\theta)$ with probability 1, where θ_κ is the actual AOA to be estimated.*

2. The AOA estimated by VAE-CIR does not necessarily minimize the angle estimation error. However, the basic design principle of VAE-CIR can be generalized to obtain the minimum mean square error (MMSE) estimator by deriving the posterior probability $P(\theta||h_\kappa(l_1)|/|h_\kappa(l_2)|)$ [21].

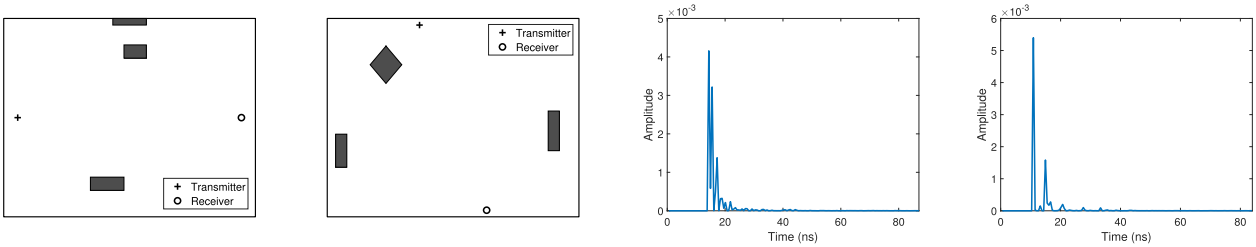

(a) Scenario A. (b) Scenario B. (c) CIR of Scenario A. (d) CIR of Scenario B.

Fig. 6. The considered scenarios and the CIR measured in these scenarios. Black blocks in the figure represent objects which could block and reflect the mmWave signals. (a) The transmitter locates at $(-2, 0)$. The receiver locates at $(2, 0)$. The three objects are characterized by $(0.1, 1, 0.4, 0.2, 0°, 3.24)$, $(-0.4, -1, 0.6, 0.2, 180°, 3.24)$, $(0, 1.45, 0.6, 0.1, 0°, 3.24)$. (b) The transmitter locates at $[-0.6, 1.4]$. The receiver locates at $[0.6, -1.4]$. The three objects are characterized by $(1.8, -0.2, 0.2, 0.6, 0°, 3.24)$, $(-2, -0.5, 0.2, 0.5, 180°, 3.24)$, $(-1.2, 0.8, 0.4, 0.4, 45°, 3.24)$. (c-d) The CIR measured in scenario A and B.

Proof. See the Appendix, which can be found on the Computer Society Digital Library at http://doi.ieeecomputersociety.org/10.1109/TMC.2020.3015936. □

Clearly, from Lemma 1, $s_\kappa^L(\theta)$ achieves its minimum at θ_κ with probability 1. In other words, if $s_\kappa^L(\theta)$ has a unique minimizer, $\widehat{\theta}_\kappa = \theta_\kappa$ and thus VAE-CIR accurately outputs the angle of interest with probability 1. This result demonstrates another advantage of VAE-CIR over existing schemes which are only based on heuristics without any performance guarantee.

Given $\widehat{\theta}_\kappa$, we are interested in whether it is an accurate estimate of θ_κ. This information is helpful since it enables us to determine, for example, whether we should collect more beam-specific measurements to refine $\widehat{\theta}_\kappa$. Without noise and non-resolvable multipath components, θ_κ should satisfies Eq. (11). Considering the potential impacts of noise and non-resolvable multipath components, we propose to determine if $\widehat{\theta}_\kappa$ is an accurate estimate of θ_κ through the following inequality:

$$\left|\frac{\left|\widehat{h}_\kappa(\underline{l})\right|}{\left|\widehat{h}_\kappa(\overline{l})\right|} - \frac{\left|G_{\underline{l}}\left(\widehat{\theta}_\kappa\right)\right|}{\left|G_{\overline{l}}\left(\widehat{\theta}_\kappa\right)\right|}\right| \leq \varepsilon, \tag{16}$$

where $\overline{l} = \arg\max_{l\in\{L-1,L\}} \widehat{h}_\kappa(l)$, $\underline{l} = \arg\min_{l\in\{L-1,L\}} \widehat{h}_\kappa(l)$, and $\varepsilon \in [0, 1]$ is a threshold. We use $\overline{l}$ and $\underline{l}$, instead of $L-1$ and L, in Eq. (16) so that we can employ the same ε no matter $\left|\widehat{h}_\kappa(L-1)\right| \geq \left|\widehat{h}_\kappa(L)\right|$ or $\left|\widehat{h}_\kappa(L)\right| \geq \left|\widehat{h}_\kappa(L-1)\right|$. The effectiveness of this criterion will be evaluated in the next section using simulations.

Remark: VAE-CIR can be easily extended to 2D arrays by replacing 2D beam pattern $G(\theta)$ in (13) with the corresponding 3D beam pattern $G(\theta, \phi)$ and searching for (θ, ϕ) which minimizes the score function defined in (13), where θ is the azimuth angle and ϕ is the elevation angle. The performance of this generalized VAE-CIR will be evaluated in Section 5.3 with the beam patterns generated from 2D arrays. Note that the math and derivation in the Appendix (available in the online supplemental material), namely, the proof of Lemma 1, can be easily extended to 2D arrays by replacing the 2D beam pattern $G(\theta)$ in the Appendix with the 3D beam pattern $G(\theta, \phi)$.

5 Performance Evaluation

5.1 Simulation Setup and Evaluation Methodology

According to [22], [23], the beam patterns of 802.11ad devices not only depend on the radiation patterns of the antenna array but also are affected by electrical components around the array. Thus, we evaluate the effectiveness of VAE-CIR with both the beam patterns generated by the Discrete Fourier Transform (DFT) codebook and those measured on the Dell D5000 docking station and the TP-Link Talon AD7200 router, which are off-the-shelf 60GHz devices with phased array antenna and beam sweeping implementation. The 32-beam patterns swept by D5000 docking stations for device discovery and the 35 default beams used by Talon routers are provided in [10] and [11]. In this evaluation, we process the measurement data in [10] and [11] so that the highest directional power gain among all beams of each device is $15dB$. Our evaluation is conducted in a $4m \times 3m$ room. The signal propagation in this environment follows the model suggested by the IEEE Task Group ad, which is validated by experimental results [24]. In this model, signal paths are generated by exploiting the clustering phenomenon in a 60GHz channel. Specifically, the first- and second-order reflections are first generated using ray-tracing techniques [25], and these paths are then blurred to generate path clusters. For each path identified via ray-tracing, a path cluster is generated by following the procedure (Section 3.7) and the parameter settings (Table 10) presented in [24]. Besides multipath propagation, the received signal is also affected by an additive Gaussian noise. We assume the CIRs are extracted from the SSW frames, and thus the preamble is generated according to the control PHY. Following [9], the signal is transmitted over a band with center frequency $60.48GHz$ and bandwidth $1760MHz$. We are interested in the AOAs of dominant paths and thus consider a receive sector sweep where the transmitter transmits SSW frames using the same beam pattern while the receiver sweeps over a set of beams to receive these SSW frames. The STF and CE field of these SSW frames are generated through Golay sequences and modulated using $\pi/2$-BPSK according to the 802.11ad standard. Once the signal is received at the receiver, we implement the channel estimation presented in Section 3 to extract the beam-specific CIR measurements, which will be used in VAE-CIR for AOA inference. It should be noted that the antenna arrays of the transmitter and the receiver are facing each other in our simulation.

In what follows, we will evaluate the performance of VAE-CIR based on the two scenarios shown in Figs. 6a and 6b where the transmitter and the receiver are characterized by their locations. We consider a coordinate system with the origin at the center of the room. The objects in the environment are characterized by six-element tuples where the first

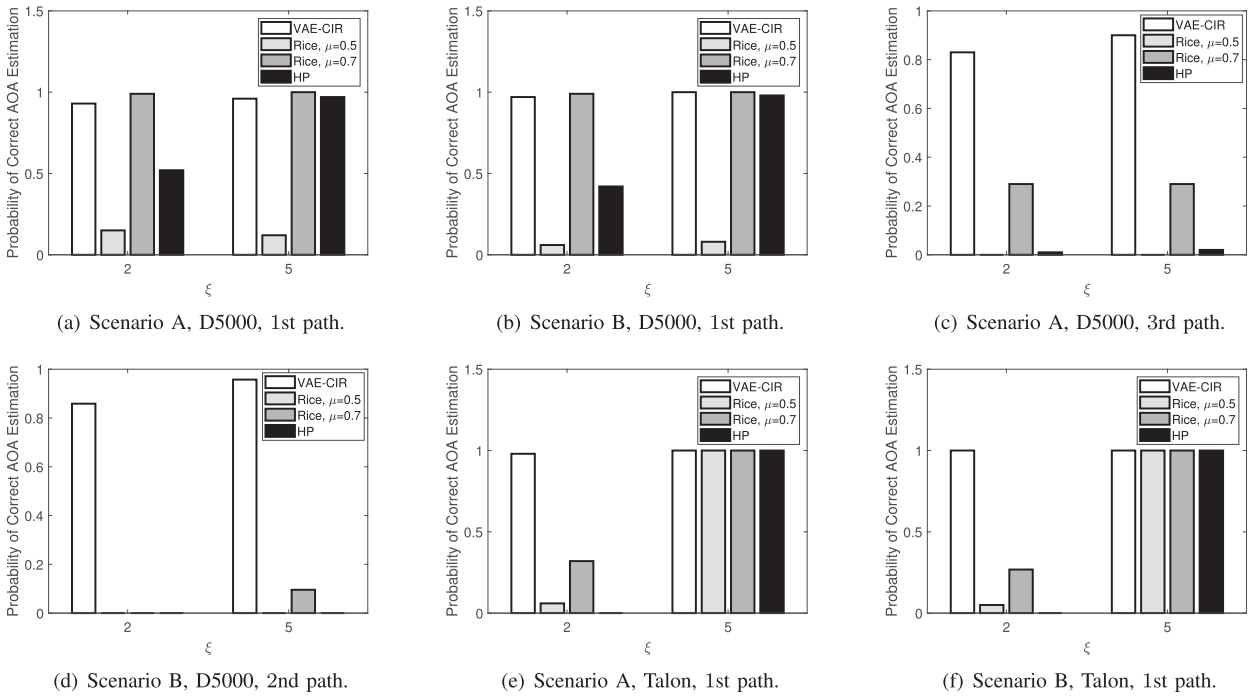

(a) Scenario A, D5000, 1st path. (b) Scenario B, D5000, 1st path. (c) Scenario A, D5000, 3rd path.

(d) Scenario B, D5000, 2nd path. (e) Scenario A, Talon, 1st path. (f) Scenario B, Talon, 1st path.

Fig. 7. The probability of correct AOA estimation in different scenarios.

two elements record their locations, the next two elements present their length and width, the fifth element is their orientation, and the last one is their dielectric constant. The examples of beam-specific CIRs extracted from these two scenarios are shown in Figs. 6c and 6d where the receiver uses the 2nd beam measured on the D5000 docking station for reception and the transmitter adopts a quasi-omni pattern with a transmit power of $25dBm$. The dielectric constant of the wall is set to 2 [26]. Form Figs. 6c and 6d, we can observe 3 peaks in Scenario A and 2 peaks in Scenario B, which correspond to dominant paths in the environment. We will take the paths/peaks identified in Figs. 6c and 6d as examples to evaluate the performance of VAE-CIR.

5.2 Result and Analysis

Fig. 7 compares the probability of correct AOA estimation of VAE-CIR with those of existing schemes. For effective comparison, we consider the angular inference schemes in [4] and [5], which are referred to as "Rice" and "HP" in Fig. 7. Similar to VAE-CIR, both of these schemes assign scores to different directions by correlating beam-specific CIR measurements with the corresponding beams in use and infer angular information based on the final scores of different directions. However, unlike VAE-CIR, they exploit absolute beam-specific CIR measurements, instead of their variations under different beams, for score updating. Besides, these two schemes always assign larger score increments to the directions with higher directional power gain, instead of the directions offering better match between the variations in CIRs and the variations in directional gains. For VAE-CIR, the threshold $\hbar$ in $\alpha(\ell, l, \kappa, \theta)$ is set to $\nu\left|\widehat{h}\right|_{\kappa}^{\max}$, where $\nu = 0.1$ and $\left|\widehat{h}\right|_{\kappa}^{\max} = \max_{l\in\{1,\cdots,L\}}\left|\widehat{h}_{\kappa}(l)\right|$. In other words, $\left|\widehat{h}_{\kappa}(l)\right|$ will be used to infer θ_{κ} only if $\left|\widehat{h}_{\kappa}(l)\right| \geq 0.1\left|\widehat{h}\right|_{\kappa}^{\max}$. For the "Rice" scheme, the κ-th dominant CIR component is considered to be detected under the lth beam if $\left|\widehat{h}_{\kappa}(l)\right| \geq \mu\left|\widehat{h}\right|_{\kappa}^{\max}$ [4]. For the "HP" scheme, the five $\left|\widehat{h}_{\kappa}(l)\right|$'s with the highest amplitudes are used for AOA inference and the estimated AOA is the center of the direction interval spanned by the five directions with highest final scores [5]. In Fig. 7, the estimated AOA $\widehat{\theta}_{\kappa}$ is considered to be accurate as long as $\left|\widehat{\theta}_{\kappa} - \theta_{\kappa}\right| \leq \xi$, where θ_{κ} is the true AOA of the κ-th path. In our experiment, the signal is transmitted at a power of $25dBm$ using the quasi-omni pattern and propagates through a multipath channel illustrated in Section 5.1. We evaluate the performance of VAE-CIR by using the beam patterns measured on different off-the-shelf 802.11ad devices (Dell D5000 docking station and TP-Link Talon AD7200 router) as the receiving beam patterns swept by the receiver.[3] Our following evaluations are based on those paths identified in Fig. 6. First, we investigate the performance of VAE-CIR in Scenario A and B with the beam patterns measured from the Dell D5000 docking station. In Figs. 7a and 7b, we present the AOA estimation results for the first dominant paths in Scenario A and B with $-30dBm$ noise in the channel. In Figs. 7c and 7d, we are interested in the AOA of the third path in Scenario A and the AOA of the second path in Scenario B, where the channel noise is set to $-40dBm$ and $-45dBm$, respectively. Then, we redo the experiment for the first paths in Scenario A and B, but, using the beam patterns measured from the Talon router. The obtained results are shown in Figs. 7e and 7f where the noise power is set to $-40dBm$. From Fig. 7, although the "Rice" and "HP" schemes achieve reasonable performance in a few cases,

3. By viewing this receiver-side beam sweeping as the transmitter-side sweeping, our experiment can also be regarded as an evaluation of the AOD estimation performance of VAE-CIR [5].

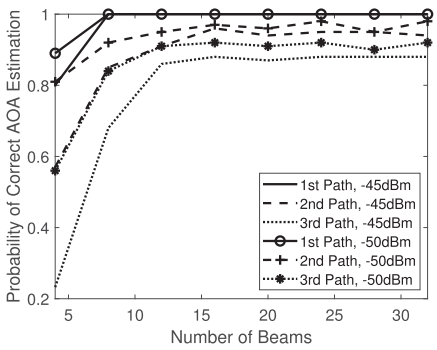

(a) Scenario A.

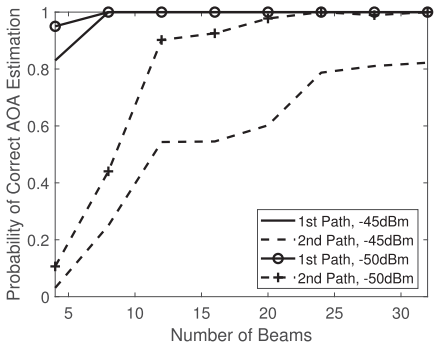

(b) Scenario B.

Fig. 8. The probability of correct AOA estimation versus additive noise and the number of beams used for CIR measurement.

they do not perform well in other cases. In contrast, VAE-CIR can achieve good AOA estimation results in all these cases, which demonstrates its effectiveness and the limited impact of nonresovable CIR components on VAE-CIR. As shown in Fig. 7, the accuracy of the "Rice" scheme highly depends on the value of μ, and both the "Rice" and "HP" schemes do not perform well for the 3rd path in Scenario A and the 2nd path in Scenario B. Compared to VAE-CIR, the main performance bottleneck of "Rice" and "HP" schemes is that their adopted score functions are not related to the AOA to be estimated. Unlike VAE-CIR, for each beam used for AOA estimation, these schemes always assign higher score increment to the direction with higher directional gain. Noticing that a higher directional gain does not necessarily mean the signal is more likely to arrive from the corresponding direction, the direction with the highest score might not necessarily be the actual AOA (these schemes output the direction with the highest score as the estimated AOA), and these schemes are likely to output an accurate AOA estimation only if the beams used for score updating have strong side lobes around the angle of interest. By examining the beam patterns of the D5000 docking station, we notice that most of its beams do not have strong side lobes around the AOAs of the 3rd path in Scenario A and the 2nd path in Scenario B, and thus the "Rice" and the "HP" schemes do not assign high enough score increments to the directions of interest, which eventually leads to inaccurate AOA estimation. In other words, since the "Rice" and the "HP" schemes assign score increments to different directions based on the absolute values of directional gains, which are not closely related to the direction of interest,

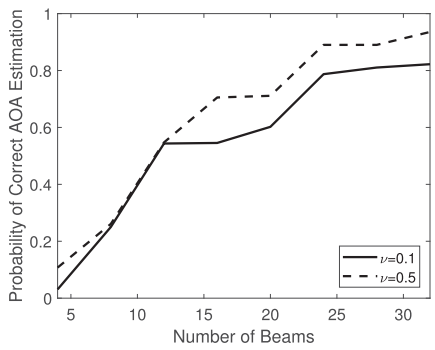

Fig. 9. The probability of correct AOA estimation versus weight factors.

their accuracy highly depends on the match between selected beam patterns and path directions. This observation further validates VAE-CIR which uses the differences between variations in $\left|\widehat{h}_\kappa(l)\right|$'s and those in directional gains, the quantities closely related to the direction of interest, for AOA estimation. When $\left|\widehat{h}_\kappa(l)\right|$ is small, the lth beam is unlikely to have strong side lobes along θ_κ. In this case, exploiting $\left|\widehat{h}_\kappa(l)\right|$ and the lth beam for score increment would lead to erroneous score increase along the direction around the strong side lobes of the lth beam. This explains why the performance of the "Rice" scheme degrades with a smaller μ.

Then, we investigate how the performance of VAE-CIR is affected by the additive noise and the number of beams used for measurement. Similar to Fig. 7, we assume the signal is transmitted at $25dBm$ using the quasi-omni pattern, and $\widehat{\theta}_\kappa$ is considered to be accurate as long as $\left|\widehat{\theta}_\kappa - \theta_\kappa\right| \leq 2$. The noise power is set to the value shown in the legend of Fig. 8. The results shown in Fig. 8 are obtained based on the 32 beams of the Dell D5000 docking station. From Fig. 8, the accuracy of AOA estimation generally improves when more beams are available for beam-specific CIR collection. With more beam-specific measurements, we could make more informative decisions and thus improve the accuracy of the AOA estimation. It can be observed from Fig. 8 that more accurate angular inference can be achieved when there is less noise in the channel. Clearly from Section 4, the accuracy of VAE-CIR depends on how accurately $\left|\widehat{h}_\kappa(l)\right|$ approximates $|h_\kappa(l)|$. The derivation in Section 3.2 shows that $\left|\widehat{h}_\kappa(l)\right|$ more accurately approximates $|h_\kappa(l)|$ when there is less noise in the channel. This explains why the performance of VAE-CIR improves with noise power decreasing. The impact of noise also can be shown through the observation that VAE-CIR achieves different accuracy for different paths. For example, for the two paths identified in Fig. 6d, we can achieve a higher probability of correct AOA estimation for the 1st path (shown in Fig. 8b). From 6d, the dominant CIR component corresponding to the 1st path is much stronger than that corresponding to the 2nd path and thus is less susceptible to noise, which eventually leads to a higher probability of correct AOA estimation. This can be further corroborated by the results in Fig. 9 where we change ν from 0.1 to 0.5 and $\widehat{h}_\kappa(l)$ will be used in score updating only when $\left|\widehat{h}_\kappa(l)\right| \geq 0.5\left|\widehat{h}\right|_\kappa^{\max}$. In so doing, weak

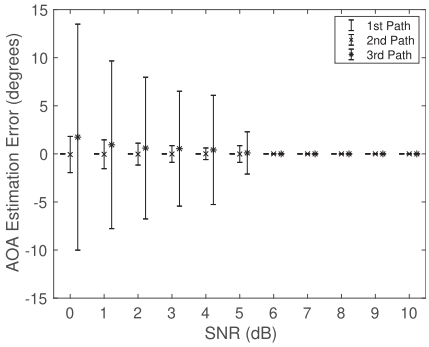

Fig. 10. The mean and standard deviation of the AOA estimation error.

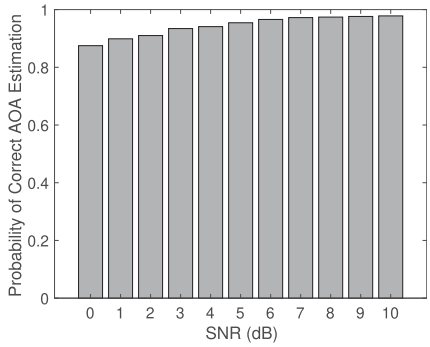

Fig. 12. The probability of correct AOA estimation in a dense environment.

$\left|\widehat{h}_\kappa(l)\right|$'s significantly distorted by noise are more likely to be excluded from AOA estimation, which reduces accumulation of noise effect and improves the probability of correct AOA estimation as shown in Fig. 9, particularly when a large number of beam-specific CIRs are used for angular inference. These observations also demonstrate the importance of introducing the weight factors $\alpha(\ell, l, \kappa, \theta)$'s to VAE-CIR. It should be noted that a large ν will not always lead to a better performance since it might limit the number of CIR measurements exploited for AOA estimation. As shown in Fig. 8, in this case, we might not be able to accurately estimate the AOAs due to limited information. In practice, the value of ν should be carefully selected. How to choose the optimal ν is out of the scope this paper and will be left for future work.

Besides the probability of correct AOA estimation, we also plot the mean and standard deviation of AOA estimation error, when VAE-CIR is applied to the three paths in Fig. 6c, as a function of received signal-to-noise-ratio (SNR) in Fig. 10. We adopt the same parameter settings as Fig. 8a, and the first 24 beams of the Dell D5000 docking station are used in our experiment. The results are presented as error bars around the mean of AOA estimation error, and the error bars in Fig. 10 represent the standard deviation of the AOA estimation error. As shown in Fig. 10, the performance of VAE-CIR improves as the SNR rises, which aligns well with the results in Fig. 8a. For the 1st and the 2nd paths, VAE-CIR can accurately estimate the AOA even if the SNR is as low as $0dB$. Compared to the 1st and 2nd paths, the 3rd path requires a higher SNR to achieve accurate AOA estimation since it is weaker as shown in Fig. 6c.

Noticing that 802.11ad also supports non-light-of-sight (NLOS) operation, we further evaluate the performance of VAE-CIR under an NLOS condition in Fig. 11. We consider the scenario in Fig. 6a with the light-of-sight (LOS) path blocked by an object located at (0,0). We apply VAE-CIR to this scenario and plot the aggregated probability of correct AOA estimation over all dominant paths in the channel in Fig. 11 as a function of received SNR. The parameter settings are the same as those in Fig. 10, and the results are obtained based on the beams of Dell D5000 docking stations. Fig. 11 shows VAE-CIR can accurately estimate the AOA even when the LOS path is blocked, which demonstrates its effectiveness under the NLOS condition.

To study VAE-CIR's performance in more dense environments, we add three more reflectors characterized by $(1, -0.5, 0.4, 0.5, 45^\circ, 3.24)$, $(-0.6, 0.5, 0.5, 0.6, -45^\circ, 3.24)$, and $(-1.5, -0.5, 0.5, 0.7, 0^\circ, 3.24)$ to the scenario shown in Fig. 6a. We apply VAE-CIR to this scenario for AOA inference and the aggregated probability of correct AOA estimation over all dominant paths in the channel is shown in Fig. 12, where we adopt the same parameter settings and set of beams as in Fig. 11. We can observe from Fig. 12 that VAE-CIR can accurately estimate the AOA with a high probability in spite of the existence of non-resolvable paths, demonstrating that non-resolvable paths have only limited effect on VAE-CIR.

In Fig. 13, we study the performance of VAE-CIR at various transmitter and receiver positions. Specifically, we consider a $4m \times 3m$ room and randomly generate 100 pairs of transmitter's and receiver's locations so that they

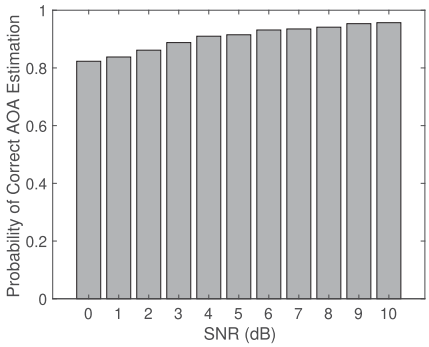

Fig. 11. The probability of correct AOA estimation under an NLOS condition.

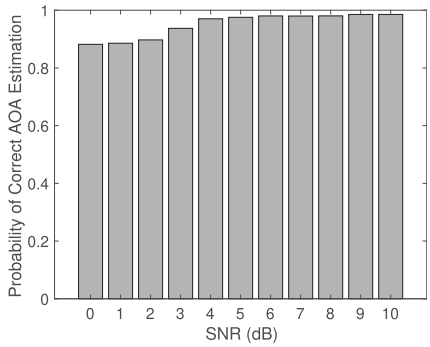

Fig. 13. The probability of correct AOA estimation under randomly distributed transmitters and receivers.

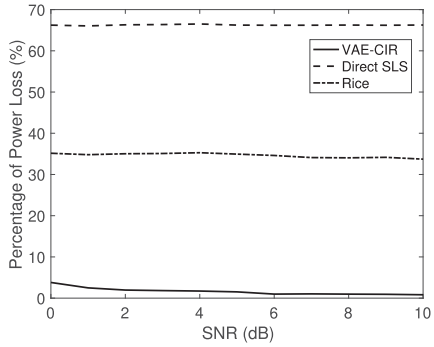

Fig. 14. The impact of different angular inference schemes on received signal power.

are at least $3m$ apart. We apply VAE-CIR to each pair of locations, and the aggregated probability of correct AOA estimation over all dominant paths identified from the 100 pairs of locations are shown in Fig. 13. In our experiment, the same parameter settings as in Section 5.1 are used and the estimated AOAs are obtained based on the beams of Dell D5000 docking station. The estimated AOA is considered to be accurate when the estimation error is within two degrees. The results in Fig. 13 show that VAE-CIR achieves accurate AOA estimation with high probability, demonstrating the effectiveness of VAE-CIR for different transmitter and receiver positions.

To further evaluate the effectiveness of VAE-CIR, we conduct a case study where the AOA estimation results of VAE-CIR are used for beam selection. Specifically, we take measurements on a set of low-resolution beams and estimate the AOA of the dominant paths based on VAE-CIR. Then, we select the high-resolution beam to be used for transmissions according to the estimated AOAs. In our evaluation, the beams of the Dell D5000 docking station are used as the low-resolution beams and the high-resolution beams are generated from an eight-element array based on the DFT codebook with half-wavelength antenna spacing. The directions of the neighboring high-resolution beams are 15° apart. We evaluate the percentage of received power loss with respect to the optimal beam selection when each of the dominant paths are used for signal propagation, and the results shown in Fig. 14 are averaged over different dominant paths. The parameter settings are the same as in Section 5.1. In Fig. 14, we also present the results when the "Rice" scheme and direct sector level sweep (SLS) are used for AOAs estimation and high-resolution beam selection. The parameter μ for the "Rice" scheme is set to 0.7. Fig. 14 shows VAE-CIR's significant performance improvement over the "Rice" scheme and SLS. From Fig. 14, the AOA estimation error of VAE-CIR results in only a small amount of loss in received signal strength and the situation improves as the received SNR during AOA estimation rises. These results further demonstrate the effectiveness of VAE-CIR.

Finally, we evaluate if the criterion introduced at the end of Section 4 can correctly determine if $\widehat{\theta}_\kappa$ is an accurate estimate of θ_κ. Specifically, we redo the simulation in Fig. 8 with $\nu = 0.1$ and the 32 beams of the D5000 docking station. Similar to Fig. 8, $\widehat{\theta}_\kappa$ is considered to be an accurate estimate of θ_κ if $\left|\widehat{\theta}_\kappa - \theta_\kappa\right| \leq 2$. Each time VAE-CIR outputs an estimated AOA, $\widehat{\theta}_\kappa$, we check if Eq. (16) is valid, with ε set to 0.3 to account for the potential impact of noise. If the inequality is valid, the criterion determines $\widehat{\theta}_\kappa$ to be an accurate estimate of θ_κ. The decisions being made is then compared to the ground truth. The results are shown in Table 1 where P_F is the percentage that the proposed criterion misclassifies $\widehat{\theta}_\kappa$ as an accurate estimate of θ_κ and P_D is the percentage that the proposed criterion correctly identify $\widehat{\theta}_\kappa$ as an accurate estimate of θ_κ. From Table 1, the criterion in Eq. (16) can accurately determine if $\widehat{\theta}_\kappa$ is an accurate estimate of θ_κ. As demonstrated in Fig. 6d, the 2nd path in Scenario B is weaker than the 1st path. Hence, for the two paths in Scenario B, the criterion in Eq. (16) is more susceptible to noise and thus less accurate when applied to the 2nd path.

TABLE 1
The Performance of the Criterion in Eq. (16)

Path \ Metric	−45dBm		−50dBm	
	P_F	P_D	P_F	P_D
Scenario A, 1st	0%	100%	0%	100%
Scenario A, 2nd	0%	99%	0%	99%
Scenario A, 3rd	2%	100%	1%	100%
Scenario B, 1st	0%	100%	0%	100%
Scenario B, 2nd	8.43%	91.57%	1.06%	98.94%

5.3 Results on 2D Arrays

At the end of Section 4, we discussed how VAE-CIR could be generalized to 2D arrays. Here we will evaluate the performance of this generalized VAE-CIR on 2D arrays. The following experiments are performed in a $4.5m \times 3m \times 3m$ room where a transmitter at $(-2, 1.25, 3)$ transmits to a receiver at (0.5,0.5,1). The beam patterns adopted in our evaluation are generated from 2D arrays based on the DFT codebook with half-wavelength antenna spacing. The neighboring beams point to directions which are $\Delta\theta$ degrees apart either in azimuth or elevation. A smaller $\Delta\theta$ results in better angular resolution, but higher overhead of beam sweeping.

Fig. 15 plots the aggregated probability of correct AOA estimation over all dominant paths in the channel as a function of received SNR. We adopt the same parameter settings as in Section 5.1, and ν in $\alpha(\ell, l, \kappa, \theta)$ is set to 0.3. The results are obtained using beams with $\Delta\theta = 10$. From Fig. 15, VAE-CIR achieves accurate AOA estimation on both 2×2 and 6×6 arrays and has a high probability of correct AOA estimation on the 6×6 array. When compared to a 6×6 array, a 2×2 array has a larger $3dB$ beamwidth, and the ratios of

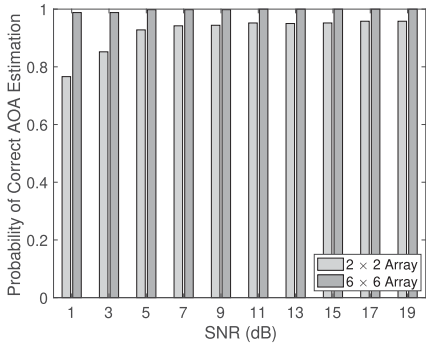

Fig. 15. The performance of VAE-CIR on 2×2 and 6×6 arrays.

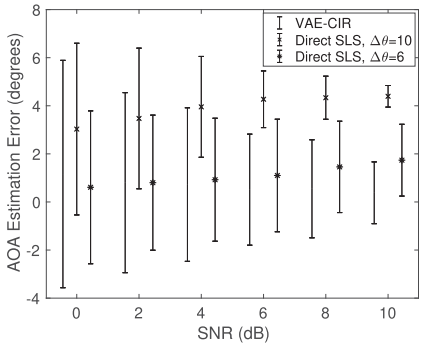

Fig. 16. The performance of VAE-CIR and direct SLS under various SNR conditions.

its beam-specific directional gains are less sensitive to the change in direction. In other words, VAE-CIR is more susceptible to noise when applying to a 2×2 array, explaining the results in Fig. 15.

Besides the probability of correct AOA estimation, we further evaluate the mean and standard deviation of the angle estimation error of VAE-CIR on a 6×6 array. The results are shown in Fig. 16 where we focus on the angle estimation error of the weakest dominant path and the results of VAE-CIR are obtained using beams with $\Delta\theta = 10$. In Fig. 16, the results are presented via error bars around the mean of estimation error, and the error bars represent the standard deviation of the estimation error. Besides VAE-CIR, the mean and standard deviation of the angle estimation error using direct SLS are also shown in Fig. 16. From Fig. 16, the performance of both VAE-CIR and direct SLS improves as the SNR increases, and VAE-CIR can achieve similar performance as direct SLS with $\Delta\theta = 6$ using beams with $\Delta\theta = 10$. In other words, when compared to SLS, VAE-CIR is less constrained by the angular resolution, $\Delta\theta$, of the beams used for angular inference. This demonstrates the superiority of VAE-CIR to SLS since, in practice, the beams swept during SLS might not be able to provide the desired $\Delta\theta$ in order to control beam-training overhead.

6 Conclusion

In this paper, we propose a direction-estimation scheme, called VAE-CIR, for 802.11ad devices by exploiting beam-specific CIR measurements. Unlike prior work, we exploit the variations between the CIRs measured under different beams, instead of their absolute values, for angular inference and prove that the performance of VAE-CIR can be guaranteed in the high SNR regime. To evaluate the performance of VAE-CIR, we have simulated the beam sweeping operation of 802.11ad devices with beam patterns measured on off-the-shelf 802.11ad devices and generated the 60GHz channel based on ray-tracing. Our evaluation results demonstrate that VAE-CIR can make more accurate angular inference for 802.11ad devices than existing schemes. We expect VAE-CIR to enable various applications, such as the link performance prediction and device tracking, on 802.11ad devices when combined with other proposals for 60GHz networking.

References

[1] T. Wei, A. Zhou, and X. Zhang, "Facilitating robust 60 GHz network deployment by sensing ambient reflectors," in *Proc. 14th USENIX Symp. Netw. Syst. Des. Implementation*, 2017, pp. 213–226.

[2] S. Sur, I. Pefkianakis, X. Zhang, and K.-H. Kim, "Towards scalable and ubiquitous millimeter-wave wireless networks," in *Proc. 24th Annu. Int. Conf. Mobile Comput. Netw.*, 2018, pp. 257–271.

[3] A. Zhou, X. Zhang, and H. Ma, "Beam-forecast: Facilitating mobile 60 GHz networks via model-driven beam steering," in *Proc. IEEE Conf. Comput. Commun.*, 2017, pp. 1–9.

[4] Y. Ghasempour, M. K. Haider, C. Cordeiro, D. Koutsonikolas, and E. Knightly, "Multi-stream beam-training for mmWave MIMO networks," in *Proc. 24th Annu. Int. Conf. Mobile Comput. Netw.*, 2018, pp. 225–239.

[5] I. Pefkianakis and K.-H. Kim, "Accurate 3D localization for 60 GHz networks," in *Proc. 16th ACM Conf. Embedded Netw. Sensor Syst.*, 2018, pp. 120–131.

[6] S. Sur, I. Pefkianakis, X. Zhang, and K.-H. Kim, "WiFi-assisted 60 GHz wireless networks," in *Proc. 23rd Annu. Int. Conf. Mobile Comput. Netw.*, 2017, pp. 28–41.

[7] S. K. Saha *et al.*, "X60: A programmable testbed for wideband 60 GHz WLANs with phased arrays," *Comput. Commun.*, vol. 133, pp. 77–88, 2019.

[8] K. Hosoya *et al.*, "Multiple sector id capture (MIDC): A novel beamforming technique for 60-GHz band multi-Gbps WLAN/PAN systems," *IEEE Trans. Antennas Propag.*, vol. 63, no. 1, pp. 81–96, Jan. 2015.

[9] *IEEE Standards 802.11ad-2012, Amendment 3: Enhancements for Very High Throughput in the 60 GHz Band*, Std. IEEE 802.11, Oct. 2012.

[10] G. Bielsa, A. Loch, I. Tejado, T. Nitsche, and J. Widmer, "60 GHz networking: Mobility, beamforming, and frame level operation from theory to practice," *IEEE Trans. Mobile Comput.*, vol. 18, no. 10, pp. 2217–2230, Oct. 2019.

[11] D. Steinmetzer, D. Wegemer, M. Schulz, J. Widmer, and M. Hollick, "Compressive millimeter-wave sector selection in off-the-shelf IEEE 802.1 lad devices," in *Proc. 13th Int. Conf. Emerg. Netw. Experiments Technol.*, 2017, pp. 414–425.

[12] I. Ahmed *et al.*, "A survey on hybrid beamforming techniques in 5G: Architecture and system model perspectives," *IEEE Commun. Surveys Tuts.*, vol. 20, no. 4, pp. 3060–3097, Fourth Quarter 2018.

[13] A. Goldsmith, *Wireless Communications*. Cambridge, U.K.: Cambridge Univ. Press, 2005.

[14] *IEEE Draft Standard P802.11-REVmd™/D3.0, Part 11: Wireless LAN Medium Access Control (MAC) and Physical Layer (PHY) Specifications*, Std. IEEE 802.11, Oct. 2019.

[15] K. V. Mishra and Y. C. Eldar, "Sub-nyquist channel estimation over IEEE 802.11 ad link," in *Proc. Int. Conf. Sampling Theory Appl.*, 2017, pp. 355–359.

[16] W.-C. Liu, F.-C. Yeh, T.-C. Wei, C.-D. Chan, and S.-J. Jou, "A digital golay-MPIC time domain equalizer for SC/OFDM dual-modes at 60 GHz band," *IEEE Trans. Circuits Syst. I, Regular Papers*, vol. 60, no. 10, pp. 2730–2739, Oct. 2013.

[17] S.-K. Yong, P. Xia, and A. Valdes-Garcia, *60GHz Technology for Gbps WLAN and WPAN: From Theory to Practice*. Hoboken, NJ, USA: Wiley, 2011.

[18] A. V. Oppenheim, A. S. Willsky, and S. H. Nawab, *Signals and Systems*, 2nd Ed. Englewood Cliffs, NJ, USA: Prentice-Hall, 1997.

[19] S. Sur, V. Venkateswaran, X. Zhang, and P. Ramanathan, "60 GHz indoor networking through flexible beams: A link-level profiling," in *Proc. ACM SIGMETRICS Int. Conf. Meas. Model. Comput. Syst.*, 2015, pp. 71–84.

[20] T. Wei and X. Zhang, "Pose information assisted 60 GHz networks: Towards seamless coverage and mobility support," in *Proc. 23rd Annu. Int. Conf. Mobile Comput. Netw.*, 2017, pp. 42–55.

[21] C. M. Bishop, *Pattern Recognition and Machine Learning*. Berlin, Germany: Springer, 2006.

[22] Y. Huo, X. Dong, and W. Xu, "5G cellular user equipment: From theory to practical hardware design," *IEEE Access*, vol. 5, pp. 13 992–14 010, Jul. 2017.

[23] B. Xu *et al.*, "Radiation performance analysis of 28 GHz antennas integrated in 5G mobile terminal housing," *IEEE Access*, vol. 6, pp. 48 088–48 101, Sep. 2018.

[24] A. Maltsev *et al.*, "Channel models for 60 GHz wlan systems," IEEE P802.11 – TASK GROUP AD Documents, doc.: IEEE 802.11-09/0334r8, May 2010.

[25] D. Steinmetzer, J. Classen, and M. Hollick, "mmTrace: Modeling millimeter-wave indoor propagation with image-based ray-tracing," in *Proc. IEEE Conf. Comput. Commun. Workshops*, 2016, pp. 429–434.
[26] E. De Groot, T. Bose, C. Cooper, and M. Kruse, "Remote transmitter tracking with raytraced fingerprint database," in *Proc. IEEE Military Commun. Conf.*, 2014, pp. 325–328.

Haichuan Ding received the BEng and MS degrees in electrical engineering from the Beijing Institute of Technology (BIT), Beijing, China, in 2011 and 2014, respectively, and the PhD degree in electrical and computer engineering from the University of Florida, Gainesville, FL, in 2018. From 2012 to 2014, he was with the Department of Electrical and Computer Engineering, University of Macau, as a visiting student. He is currently a professor with the School of Cyberspace Science and Technology, Beijing Institute of Technology, Beijing, China. His current research interests include mmWave and V2X communications.

Kang G. Shin (Life Fellow, IEEE) received the BS degree in electronics engineering from Seoul National University, Seoul, Korea, and the MS and PhD degrees in electrical engineering from Cornell University, Ithaca, New York, in 1970, 1976, and 1978, respectively. He is the Kevin and Nancy O'Connor professor of computer science and Founding director of the Real-Time Computing Laboratory with the Department of Electrical Engineering and Computer Science, The University of Michigan, Ann Arbor, Michigan. At Michigan, he has supervised the completion of 85 PhDs and also chaired the Computer Science and Engineering Division for three years starting in 1991. From 1978 to 1982 he was on the faculty of the Rensselaer Polytechnic Institute, Troy, New York. His current research focuses on QoS-sensitive computing and networks as well as on embedded real-time and cyber-physical systems. He has authored/coauthored close to 1000 technical articles (more than 350 of which are published in archival journals) and more than 50 patents or invention disclosures. He has also received numerous institutional awards and best paper awards. He is fellow of ACM.